



This is a repository copy of *Enhancing soft-magnetic properties of Fe-based nanocrystalline materials with a novel double-scanning technique*.

White Rose Research Online URL for this paper:

<https://eprints.whiterose.ac.uk/204510/>

Version: Published Version

Article:

Özden, M.G. orcid.org/0000-0002-1067-8881 and Morley, N.A. (2023) Enhancing soft-magnetic properties of Fe-based nanocrystalline materials with a novel double-scanning technique. *Advanced Engineering Materials*, 25 (22). 2300700. ISSN 1438-1656

<https://doi.org/10.1002/adem.202300700>

Reuse

This article is distributed under the terms of the Creative Commons Attribution-NonCommercial-NoDerivs (CC BY-NC-ND) licence. This licence only allows you to download this work and share it with others as long as you credit the authors, but you can't change the article in any way or use it commercially. More information and the full terms of the licence here: <https://creativecommons.org/licenses/>

Takedown

If you consider content in White Rose Research Online to be in breach of UK law, please notify us by emailing eprints@whiterose.ac.uk including the URL of the record and the reason for the withdrawal request.



eprints@whiterose.ac.uk
<https://eprints.whiterose.ac.uk/>

The Relevance of Measurement Systems Analysis

A Procter & Gamble Case Study on
MSA Methodology and Applications

DATE

**OCTOBER
10 AND 12**

TIME

**16:00 CET,
10 am EST**



**CHRISTIAN
NEU**

Scientist
Procter & Gamble



**JERRY
FISH**

Systems Engineer
JMP



**JASON
WIGGINS**

Senior Systems
Engineer
JMP

Register now

Enhancing Soft-Magnetic Properties of Fe-Based Nanocrystalline Materials with a Novel Double-Scanning Technique

Merve G. Özden* and Nicola A. Morley

This article presents a novel scanning technique for the laser powder bed fusion (LPBF) of Fe-based soft-magnetic alloys, which have low glass forming ability, and microstructural change happens during LPBF process. This technique involves double scanning where 1) the first scan applied uses high energy density ($E = P/vht$, where P is the laser power, v is the laser scan speed, h is the hatch spacing, and t is the layer thickness) with different process parameters (P : 30, 40, and 50 W, v : 500, 600, and 700 mm s⁻¹, h : 20 and 30 μm, and t : 50 μm) to achieve high density and 2) the second scan employed before the spreading subsequent powder layer uses low E ($=20$ J mm⁻³, $P = 20$ W, $v = 1000$ mm s⁻¹, $h = 20$ μm, and $t = 50$ μm) to refine the microstructure and thus reduce coercivity. This increases the saturation magnetization to a maximum value of 226.81 Am² kg⁻¹ and reduces the coercivity to a lowest value recorded (130 A m⁻¹). Likewise, the bulk density (94.59–99.25%) is enhanced significantly with double scanning, especially the samples produced using high P (50 W) resulting from the relieving of the mechanical and thermal stress evolving during the process.

1. Introduction


Soft-magnetic alloys have been playing a critical role in power generation, transformation, and energy conversion, making them a significant engineering material for both industry and academia.^[1–6] The excellent efficiency and low core loss demonstrated by Fe-based soft magnetic bulk metallic glasses (BMGs) have generated immense interest in their use as core materials in power electronics and industrial transformers.^[1,7] Soft magnetic BMGs lack crystal structures or long-range orders, resulting in no magnetocrystalline anisotropy energy.^[8] In contrast, nanocrystalline soft magnetic alloys have reduced effective

magnetocrystalline anisotropy energy and thus low hysteresis loss.^[9–11] They are typically produced using planar flow casting techniques, with a thickness range of 15–30 μm and composed of fully or partially amorphous phases. These alloys are also referred to as metal amorphous nanocomposites.^[12] Fe-based amorphous ribbons have higher electrical resistivity of 1.0–1.3 μΩm compared to silicon steels due to their lack of long-range orders, contributing to lower eddy current loss.^[5] Nevertheless, their saturation polarization (J_s) is relatively inferior in comparison to that of silicon steel. Developing Fe-based BMGs with high J_s and low core loss is crucial for enhancing the power density and efficiency of advanced electronic devices.^[2] Various approaches have been taken to increase the J_s of Fe-based BMGs, such as the modifying compositions^[13,14] and

nanocrystallization.^[15] However, the composition modulation by increasing Fe content and adjusting metalloid elements has limitations due to the trade-off between J_s and glass forming ability.^[16] Co substitution has been found to be effective in improving J_s without reducing the glass forming ability,^[17,18] but it can bring about increased magnetic anisotropy and Curie temperature (T_c), along with worsening magnetic softness.^[19] Nanocrystallization encounters difficulties in the producibility as generally Fe-based nanocrystalline alloys having high J_s cannot be manufactured into application-level sized parts resulting from the low glass forming ability.^[17,20]

Fe-based soft magnetic nanocrystalline alloys, containing nano-scale phases embedded in the amorphous matrix, offer various benefits: 1) the presence of the α -Fe phase provides high saturation magnetization (M_s),^[16,21] 2) superior magnetic softness contributes to low core loss (1/10–1/4 of the commercial silicon steels),^[1,22–25] and 3) the dual-phase coupling results in low magnetostriction and super-high permeability (Figure 1).^[6,9,26–28] Furthermore, as the structural correlation length of nanocrystalline alloys is less than the exchange correlation length of the magnetic spins, the magnetocrystalline anisotropy (K_1) is averaged out over the randomly oriented grains, leading to a low coercivity (H_c).^[29–32] Fe-based nanocrystalline alloys are typically produced upon crystallization from an amorphous matrix through various methods, such as single roller spinning followed by annealing,^[3] consolidation (hot pressing) of mechanically alloyed powder,^[33] and ultrafast high-energy ball milling.^[34,35]

M. G. Özden, N. A. Morley
Department of Material Science and Engineering
University of Sheffield
Sheffield S1 3JD, UK
E-mail: mgozden1@sheffield.ac.uk

 The ORCID identification number(s) for the author(s) of this article can be found under <https://doi.org/10.1002/adem.202300700>.

© 2023 The Authors. Advanced Engineering Materials published by Wiley-VCH GmbH. This is an open access article under the terms of the Creative Commons Attribution-NonCommercial-NoDerivs License, which permits use and distribution in any medium, provided the original work is properly cited, the use is non-commercial and no modifications or adaptations are made.

DOI: 10.1002/adem.202300700

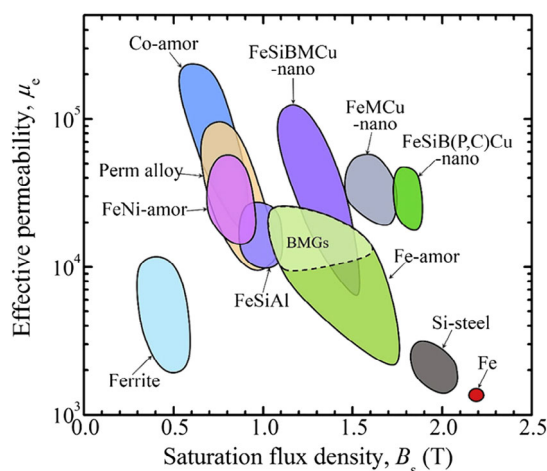


Figure 1. The graph showing the relations between effective permeability at 1 kHz and saturation flux density of soft-magnetic materials. Reproduced with permission.^[53] 2022, AIP Publishing.

The current techniques for producing Fe-based soft-magnetic alloys are limited by the material's glass forming ability, dimensional limitations, and the geometric complexity. Laser powder bed fusion (LPBF) technology, which uses a laser to consolidate powders in a layer-by-layer manner, can overcome these limitations. Achieving high cooling rates (up to $10^6\text{--}10^8\text{ K s}^{-1}$) during this process makes it a good option for fabricating Fe-based amorphous/nanocrystalline alloys with complex shapes.^[36–38] However, controlling microstructure is challenging due to the complex thermal nature of the process. Researchers are using various methods to improve the quality of the LPBF-processed samples, such as optimizing process parameters and using multiscanning strategies. The degree of amorphization of the resulting material is an important factor for Fe-based amorphous/nanocrystalline materials. To increase the amorphous content and keep crystallite size of the α -Fe phase minimal ($<20\text{ nm}$), crystallization must be suppressed during both the cooling of the molten metal and the absorption of the melt's heat by the previously solidified part.^[39] For this purpose, researchers have utilized different scanning strategies to build 3D parts with reduced crystallinity. The initial approach involved performing two laser scans to each layer before spreading the subsequent layer, which allowed the scientists to process Fe-based amorphous/nanocrystalline alloy with M_s of 1.22 T and high density of 96%.^[40] This method also increased the amorphization degree to 47% and decreased the coercivity. Another approach involved a two-stage laser scanning process: pre-laser melting followed by short-pulse laser treatment to induce amorphization.^[41] This strategy fabricated a sample with a maximum relative density of 94.1% and an amorphous phase content of 89.6%. Although this research succeeded in increasing the amorphous phase content, bulk density ($>99\%$) and soft-magnetic properties (high M_s ($<1.5\text{ T}$) and low H_c ($<1\text{ kA m}^{-1}$)), it still needs improvement. With this aim, a novel scanning strategy was introduced to LPBF-process Fe-based nanocrystalline soft-magnetic alloys to control the microstructure during the process.

2. Experimental Section

2.1. Materials

For this study, the commercial FeSiBCrC amorphous powder, provided by Epson Atmix Corporation, Japan, was used with the elemental compositions of 87.38 (Fe), 6.85 (Si), 2.54 (B), 2.46 (Cr), and 0.77 (C) in mass %. The Fe–Si–B–Cr–C system is more readily available and sustainable compared to other competitive materials, which contain Co or rare-earth materials such as Nd and Dy. The only high-priced element is boron, which is present in a smaller quantity (2.54%) compared to other Fe-based amorphous/nanocrystalline alloys. Carbon contributes to the glass forming ability of the alloy due to being small atom like B and Si. On the other hand, chromium is a cheaper alternative to the Cu and Nb atoms, preventing the growth of crystallites. The powder characterization was presented in our previous work,^[42] which indicated that the powder was fully amorphous, spherical in shape, and has a narrow particle size distribution with D10, D50, and D90 of 9.49, 23.4, and 47.5 μm , respectively. Additionally, it exhibits soft-magnetic behavior, with M_s of $102\text{ Am}^2\text{ kg}^{-1}$ and H_c of 2.27 kA m^{-1} .

2.2. Methods

To begin with, the powder was sifted through a sieve with a mesh size of $53\text{ }\mu\text{m}$ to narrow the size distribution of the particles, which will aid in their spreadability and flowability over the powder bed. A cylindrical sample with a diameter of 6 mm and a height of 5 mm was then printed using an Aconity Mini machine. From the main laser process parameters, low laser powers ($P = 30, 40, \text{ and } 50\text{ W}$) were utilized to increase cooling rate and inhibit crystallization. On the other hand, it was indicated in our previous works^[42,43] that energy density ($E = P/vht$, where v is the laser scan speed, h is the hatch spacing, and t is the layer thickness) must be higher than 45 J mm^{-3} to obtain high bulk density ($>97\%$). In order to increase energy density, relatively low laser scan speeds ($v = 500, 600, \text{ and } 700\text{ mm s}^{-1}$) and hatch spacing ($h = 20 \text{ and } 30\text{ }\mu\text{m}$) were exploited with the layer thickness being kept constant at $t = 50\text{ }\mu\text{m}$. For the first scan, a combination of the different laser process parameters was used to achieve energy density values within the range $42.86\text{--}100\text{ J mm}^{-3}$, to build 3D parts with high density; these are presented in **Table 1**. The second scan with a low energy density ($E = 20\text{ J mm}^{-3}$, $P = 20\text{ W}$, $v = 1000\text{ mm s}^{-1}$, $h = 20\text{ }\mu\text{m}$, and $t = 50\text{ }\mu\text{m}$) was applied to each powder layer before spreading the subsequent layer. The reasons for this were 1) to provide thermal stress relaxation, eliminating residual stress in the microstructure, 2) to decrease the crack density in the

Table 1. The process parameters used in the first laser scan.

$E\text{ [J mm}^{-3}\text{]}$	$h = 20\text{ }\mu\text{m}$			$h = 30\text{ }\mu\text{m}$
	$P = 30\text{ W}$	$P = 40\text{ W}$	$P = 50\text{ W}$	$P = 50\text{ W}$
$v = 500\text{ mm s}^{-1}$	60	80	100	66.67
$v = 600\text{ mm s}^{-1}$	50	66.67	83.33	55.56
$v = 700\text{ mm s}^{-1}$	42.86	57.14	71.43	47.62

microstructure, and 3) to refine the microstructure by introducing nanosized α -Fe(Si) crystallites within the microstructure, which should eventually increase the saturation magnetization (M_s) and lower the coercivity (H_c). In addition, the specimens were produced using the hatch filling technique, with a starting angle of 22.5° and a rotation of 70° after each layer. To avoid oxidation, the residual oxygen content in the chamber was kept below 0.01%.

For characterization, the Archimedes technique was employed to measure the densities of the printed samples thrice using distilled water. To determine the bulk density percentage, the mean density and theoretical density (7.294 gr cm^{-3}) were used for each sample. For the microstructural imaging, each sample was subjected to grinding, polishing, and etching for 3 min using a 2% nital solution (98 mL HNO_3 and 2 mL ethanol).

The micrographs were captured using INSPECT F50 HR-SEM (high-resolution scanning electron microscope). The crystallite sizes of α -Fe(Si) phases and the melt-pool zone percentage within the microstructure were measured using the ImageJ program from the SEM microstructures. Finally, the soft-magnetic properties (M_s and H_c) were determined from the magnetization hysteresis ($M-H$) loops obtained via a SQUID magnetometer MPMS3 from Quantum Design, with fields up to 160 kA m^{-1} at 300 K.

3. Results and Discussion

The development of the microstructure in Fe-based amorphous/nanocrystalline alloys during the LPBF procedure is a

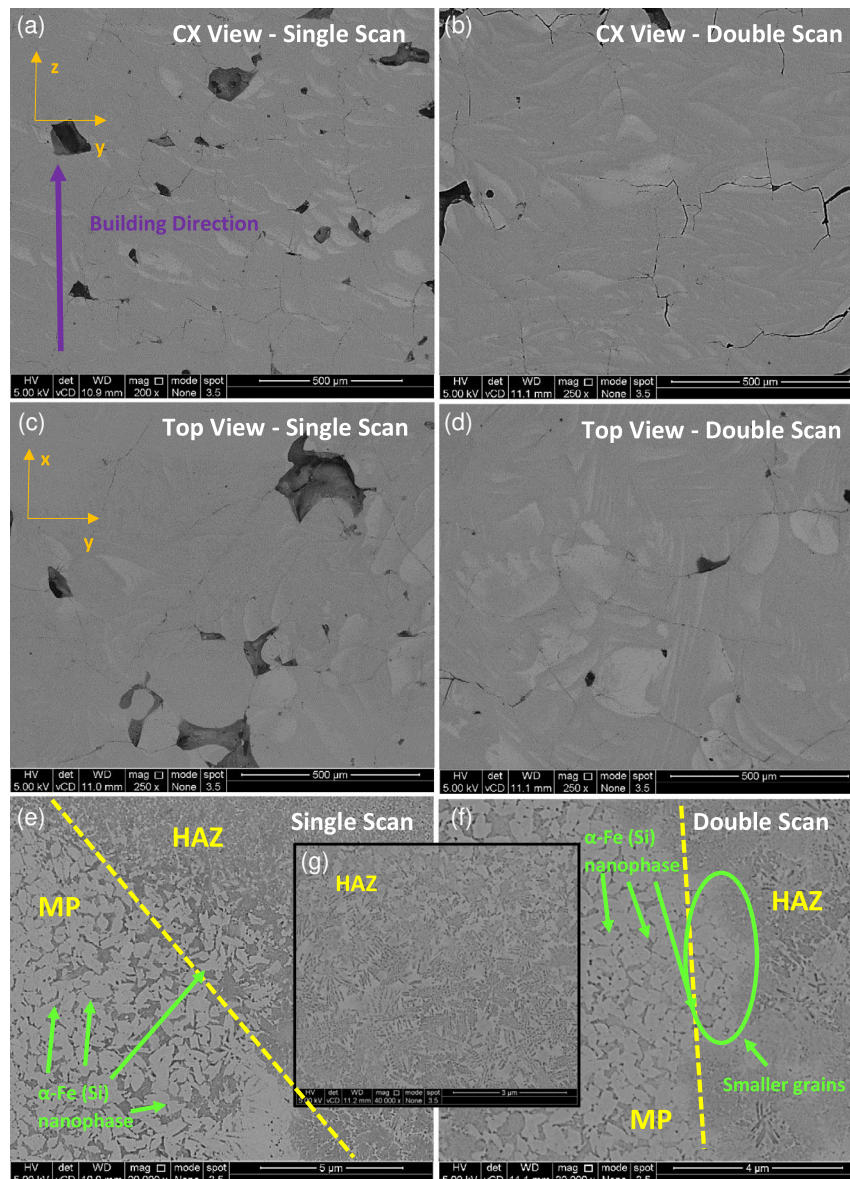


Figure 2. The SEM micrographs of the sample produced with P of 50 W , v of 500 mm s^{-1} , h of $20 \mu\text{m}$, and t of $50 \mu\text{m}$ a–d) at low magnification showing melt-pool (MP) region (lighter areas) and heat-affected zone (HAZ) (darker areas); e,f) at high magnifications illustrating α -Fe(Si) phase with different size within the MP region; and g) at high magnification showing star-like growth of Fe_3Si phase within HAZ (CX means cross-sectional).

complicated process due to the heterogeneous nature of the thermal evolution. The microstructure can be divided into two regions: molten pools (MP) and heat-affected zone (HAZ), both of which experience different cooling rates resulting in distinct microstructures. In **Figure 2**, darker gray areas represent HAZ, whereas lighter gray areas denote MP. The cooling rate decreases from the MP region to the HAZ because of the formation of high thermal gradients during laser scanning. It is well known that the growth of the ordered Fe_3Si phase is star-like, whereas the disordered $\alpha\text{-Fe(Si)}$ phase appears as equiaxial grains in the microstructure.^[41] In addition, phase identification (XRD and TEM analysis) was presented in our previous article.^[42] In the MP region, $\alpha\text{-Fe(Si)}$ nanograins with varying sizes were observed, while the HAZ mainly contains Fe_3Si nanocrystalline clusters (Figure 2e–g). The MP region provides more supercooling, enabling the nucleation and growth of the disordered $\alpha\text{-Fe(Si)}$ phase. The grains in the MP were found to be coarser than those in the HAZ due to decreased nucleation rates and increased growth velocity resulting from a high driving force for atomic diffusion.^[44] This ultimately leads to grain coarsening.

In general, even though the cooling rate of the Fe-based BMGs in LPBF process is a lot higher than their critical cooling rate, some regions in the microstructure will experience low temperatures ($<T_g$ (glass transition temperature)) or very short exposure time to heat input, leading to mechanical stress, contamination, prolonged thermal exposure, and thermal cycling, which are the major reasons to promote nucleation.^[45,46] As it can be seen in the microstructures (Figure 2), the samples possess pores and cracks, which act as nucleation sites and facilitate heterogeneous nucleation. Although large metallurgical pores in Figure 2a,c seem to be eliminated with the help of double scanning (Figure 2b,d), the crack density was observed to be not affected by this new technique. Those large pores resulted from the lack of fusion, which occurs when the powder bed does not receive sufficient heat input owing to low laser power (50 W), creating a gap between layers. Double scanning improved the bulk density significantly (**Figure 3**), especially at the relatively higher laser power ($P = 50$ W). Furthermore, increasing P influences the bulk density more than laser scan speed (v) and hatch spacing (h), which did not change the porosity level enormously. This is because the laser power is a critical parameter for

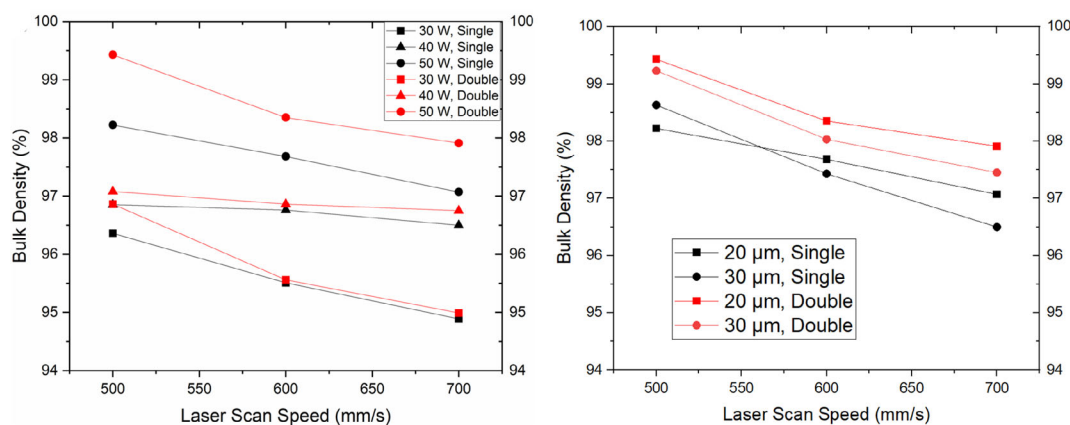


Figure 3. Bulk density values as a function of laser scan speed. Left image shows the effect of laser power (30, 40, and 50 W) and double scan (hatch spacing is constant and 20 μm) whereas the right image indicates the influence of hatch spacing (20 and 30 μm) and double scan (laser power is constant and 50 W).

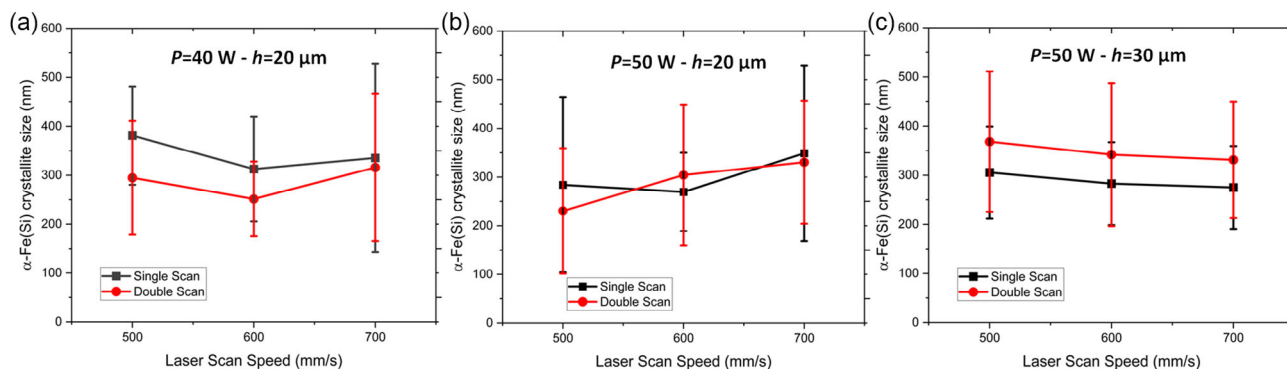


Figure 4. The graphs of $\alpha\text{-Fe(Si)}$ crystallite size versus laser scan speed, showing the mean crystallite sizes with the square and circle symbols and the particle size distribution with the error bars: a–c) illustrate the crystallite sizes of the samples produced with laser power (P) of 40 W - hatch spacing (h) of 20 μm , P of 50 W - h of 20 μm , and P of 50 W - h of 30 μm , respectively.

complete melting and consolidation of powder particles. Increasing v and h deteriorates the bulk density as high v causes short exposure time in the powder bed and high h increases the overlapping distance between MPs.

The saturation magnetization (M_s) values of the printed samples, range from 160 to 230 Am² kg⁻¹ (Figure 4), are comparable to the other LPBF-processed Fe-based nanocrystalline materials (150–199 Am² kg⁻¹).^[41,47–50] M_s of soft-magnetic nanocrystalline alloys depends strongly on the fraction of crystalline and amorphous phases, the crystalline phase amount, and the alloy composition with the amount of magnetic transition metals (Fe, Co, and Ni) being the most influential factor.^[51] In all 3D-printed samples, the alloy composition is identical, and thus, the M_s values differ based on the amount of the α -Fe(Si) phase throughout the samples.

Typically, Fe-based nanocrystalline alloys show superior soft-magnetic behavior when they contain fine α -Fe nanocrystallites (10–15 nm) embedded into an amorphous matrix, separated by 1–2 nm for exchange interaction, with H_c ranging from 0.4 to 8 Am⁻¹, and M_s values reaching up to 1.3 T (≈ 1000 kA m⁻¹).^[52] In this study, the saturation induction (B_s) can go up to 2 T (≈ 1500 kA m⁻¹), probably owing to the larger mean crystallite size (>200 nm) of the α -Fe(Si) phases and their higher amount within the microstructure. As stated before, the size of α -Fe(Si) crystallite varies in MP, increasing from the end of the HAZ through the center (Figure 2e,f). For this reason, it deviates significantly from the mean value (Figure 4). It should be noted that particle size distribution throughout the MP zone was drawn as a histogram (exactly as shown in Figure 6), from which the mean and standard deviation of the particle size distribution were obtained. The error bars in Figure 4 symbolize this standard deviation, not the one resulting from the errors in measuring; they simply show how much the crystallite sizes fluctuate within the MP region. The mean values are shown as circle and rectangle symbols in Figure 4. Also, to predict the content of α -Fe(Si) phase in the microstructure, the percentage of the MP zone (Figure 5) was quantified from low-magnification SEM

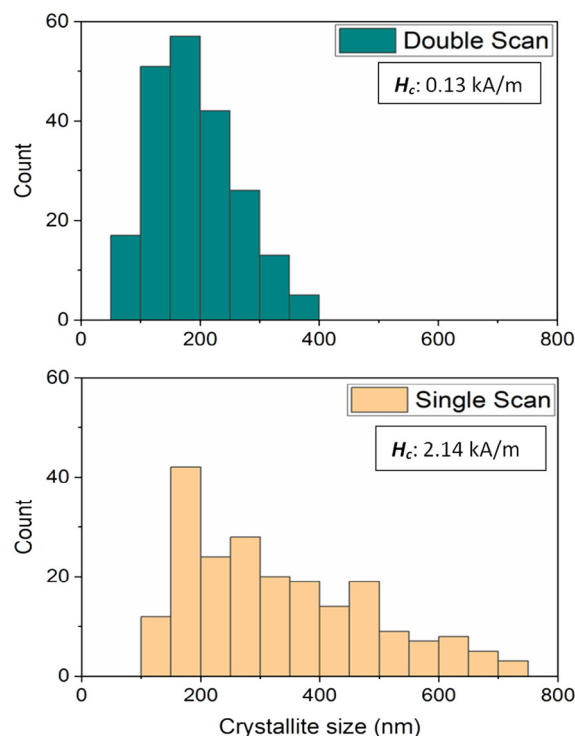


Figure 6. The histograms showing particle size distribution of α -Fe(Si) phase in the MP region with different processing conditions (single scan and double scan). The sample was processed with laser power of 30 W, hatch spacing of 20 μ m, and laser scan speed of 500 mm s⁻¹.

micrographs, assuming that lighter gray regions in Figure 2 exhibit only α -Fe(Si) phase.

Before discussing microstructural change with different process parameters, thermal development from MP through HAZ is needed to be mentioned. In our previous study, the thermal modeling indicated that higher v , lower P , and h lead to higher

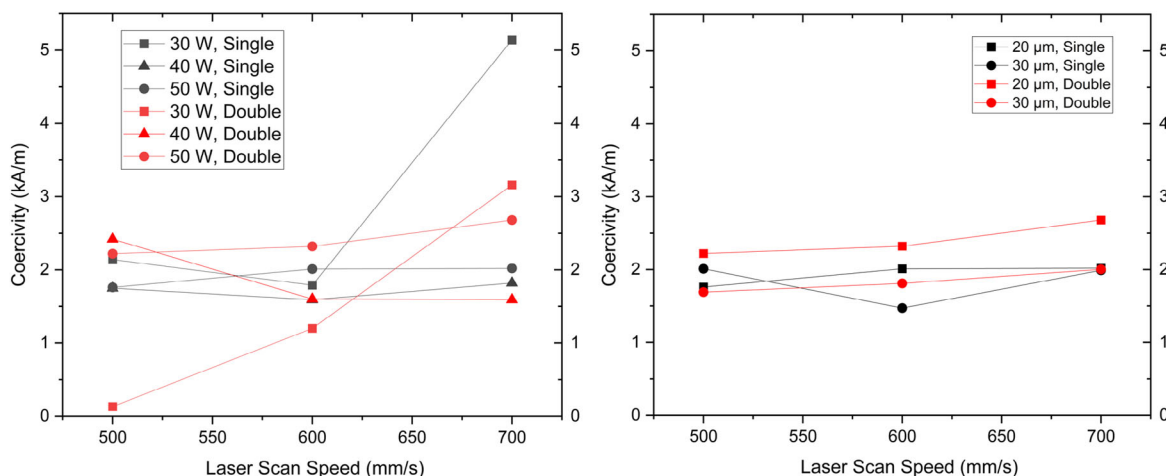


Figure 5. Coercivity values as a function of laser scan speed. Left Image shows the effect of laser power (30, 40, and 50 W) and double scan (hatch spacing is constant and 20 μ m), whereas the right image indicates the influence of hatch spacing (20 and 30 μ m) and double scan (laser power is constant and 50 W).

cooling rate and only P influences thermal gradient; the lower the laser power, the higher the thermal gradient.^[43] Based on this modeling, the second scan (with parameters $P = 20$ W, $v = 1000$ mm s⁻¹, and $h = 20$ μ m) exhibits the highest cooling rate ($>10^7$ K s⁻¹) and thermal gradient ($>10^7$ K m⁻¹). Nonetheless, when it comes to the process parameters of the first scan, there is not much variation (cooling rate: 7.26×10^6 K s⁻¹– 1.01×10^7 K s⁻¹ and thermal gradient: 1.38×10^7 K m⁻¹– 1.48×10^7 K m⁻¹). For this reason, the crystallite size exhibited minimal change across the various process parameters (as shown in Figure 4), resulting in a nearly consistent coercivity ranging between 1.5 and 2.5 kA m⁻¹ (as depicted in Figure 5), primarily influenced by the crystallite size.^[30] The only notable difference is observed at the initial scan of $P = 30$ W and $v = 500$ mm s⁻¹ together with the double scan.

This work has successfully produced a LPBF-processed sample with the lowest coercivity recorded (130 A m⁻¹) using a low laser power (30 W) and double scanning (Figure 6). The reason for this is that the sample has a finer grain size with a narrow particle size distribution (191.01 ± 72.15 nm, mean \pm standard

deviation of the particle size distribution) compared with that of the single scan sample (348.55 ± 176.44 nm, mean \pm standard deviation of the particle size distribution).

The saturation magnetization mostly depends on the α -Fe(Si) phase content within microstructure in this study as this phase possesses the highest magnetization and larger crystallites. Other phases were excluded from consideration when investigating the impact of process conditions on magnetic properties. The quantification of the MP zone percentage (as depicted in Figure 7) was performed using low-magnification SEM micrographs, under the assumption that regions appearing lighter in gray in Figure 2 exclusively represent the α -Fe(Si) phase. It was found that the process parameters of $v = 500, 600$ mm s⁻¹ and $h = 30$ μ m (Figure 7b) have the highest proportion of MP zone ($>50\%$). Larger h (30 μ m) increases the melt-pool overlapping distance, which reduces the amount of HAZ. The effect of v can be attributed to the cooling rate; at $v = 600$ mm s⁻¹, the cooling rate is always in the range of $8.57 - 8.63 \times 10^6$ K s⁻¹, which may be the ideal thermal condition for the formation of α -Fe(Si) phase. Additionally, this may explain why double scanning led to

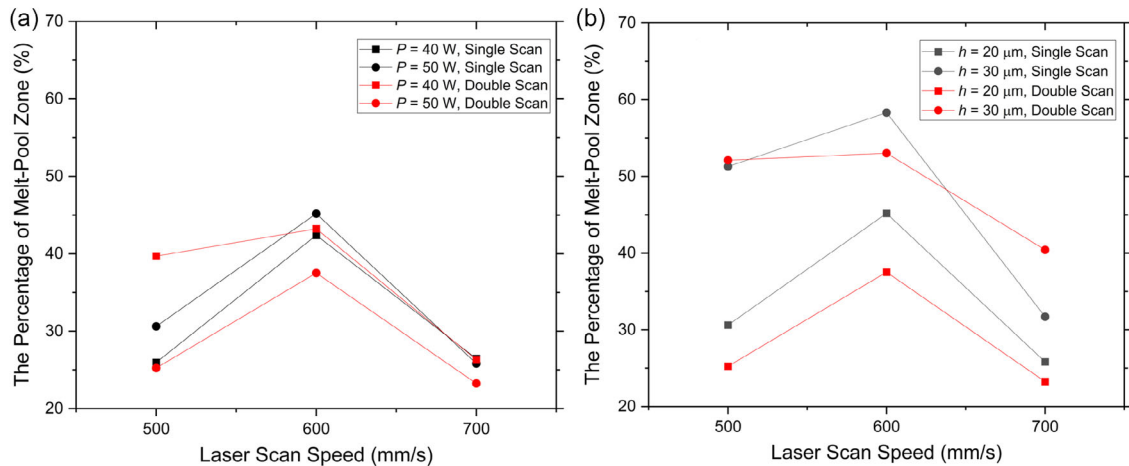


Figure 7. The graphs of the percentage of MP zone as a function of laser scan speed, showing the effect of single and double scan: a) laser power and b) hatch spacing on the MP zone amount within the microstructure.

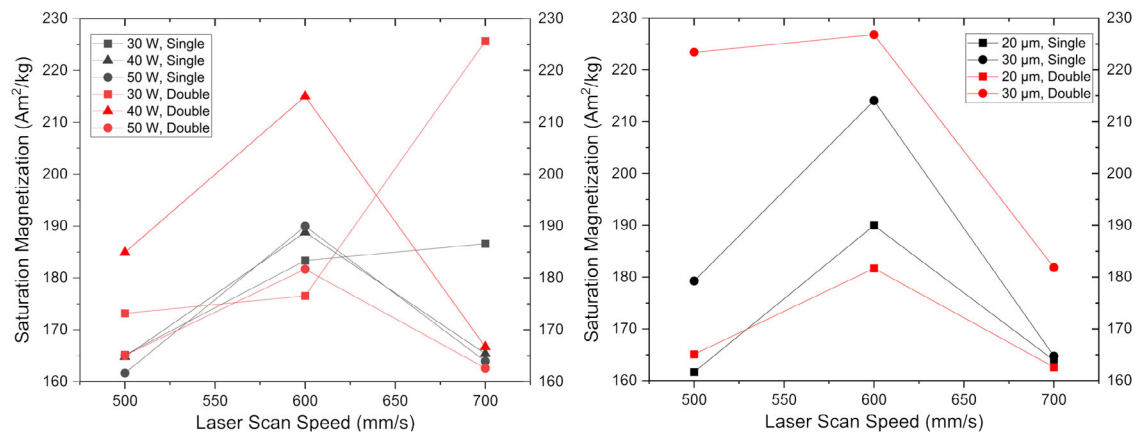


Figure 8. The graphs of saturation magnetization versus laser scan speed. Left Image shows the effect of laser power (30, 40, and 50 W) and double scan (hatch spacing is constant and 20 μ m), whereas the right image indicates the influence of hatch spacing (20 and 30 μ m) and double scan (laser power is constant and 50 W).

a slight reduction in the percentage of the MP zone. **Figure 8** indicates that the saturation magnetization (M_s) is also at its highest when the laser scan speed is 600 mm s^{-1} and hatch spacing is $30 \mu\text{m}$. This suggests that M_s was mainly affected by the amount of MP within the microstructure.

In order to comprehend the relationship between the proportion of MP zone and M_s , the graph in **Figure 9** was made, revealing that there is an almost linear tendency of increasing M_s with increasing the MP amount. According to this graph, to achieve high M_s ($>200 \text{ Am}^2 \text{ kg}^{-1}$), the MP percent needs to be at least 40%. In addition, the relationship between coercivity and mean crystallite size is presented in **Figure 10**. This graph complies with Herzer's grain size dependent-coercivity graph,^[9–11,29,30] at which below $D = 200 \text{ nm}$, there is sharp decrease in coercivity

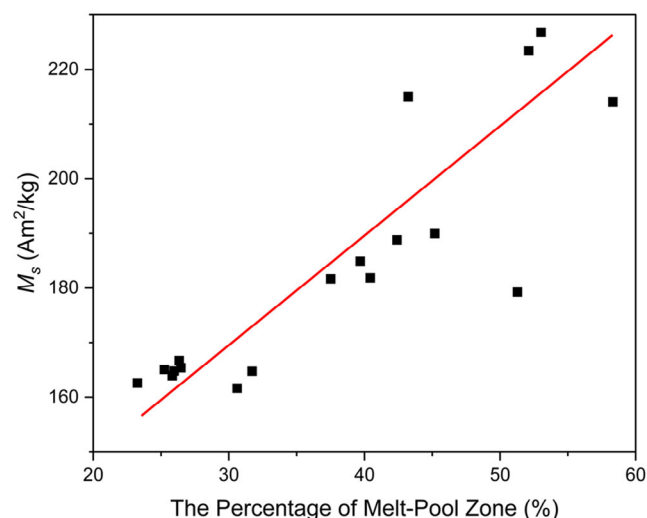


Figure 9. The graph of saturation magnetization versus the percentage of MP zone within the microstructures of LPBF-processed samples.

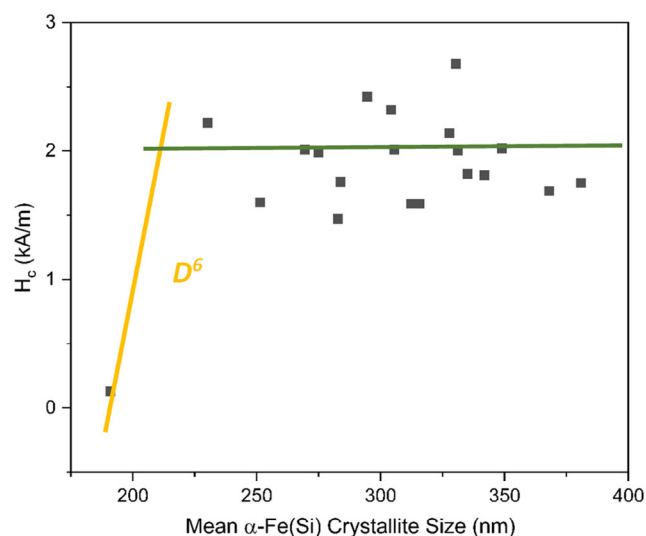


Figure 10. The graph of coercivity versus mean $\alpha\text{-Fe(Si)}$ crystallite size within the MP zone in the microstructure (D denotes grain (crystallite) size).

to near-zero, proportional with D^6 and after that point, coercivity is nearly constant (2 kA m^{-1}) till around $D = 600 \text{ nm}$.

4. Conclusion

This study introduced a newly developed scanning technique to improve the soft-magnetic properties of LPBF-processed Fe-based amorphous/nanocrystalline alloys with varying laser process parameters. This technique involved the first scan with high E (the combination of different laser process parameters) to obtain the 3D parts with high bulk density, followed by a second scan with low E before the spreading of the subsequent powder layer. This was done to decrease the coercivity by decreasing the crystallite size below 200 nm . With this new technique, the lowest coercivity (130 A m^{-1}) was successfully achieved using the LPBF process. The double-scan technique also improved the bulk density ($<99.5\%$) and the saturation magnetization ($<230 \text{ Am}^2 \text{ kg}^{-1}$). The particle size distribution of the $\alpha\text{-Fe(Si)}$ phase (main phase in the microstructure) and melt-pool percentage were also quantified to understand the magnetization mechanism that the 3D printed samples undergo. The investigation revealed that process parameters of $v = 500$ and 600 mm s^{-1} , along with $h = 30 \mu\text{m}$, resulted in the highest proportion of the MP zone ($>40\%$). This enhanced the M_s ($>200 \text{ Am}^2 \text{ kg}^{-1}$). Also, low P (30 W) along with double scanning reduces the coercivity to the lowest recorded value (130 A m^{-1}) by decreasing grain size below 200 nm . The new technique has led to a higher M_s , bulk density, and the lowest H_c value (for the LPBF process). A reduction in the amount of defects like cracks and pores is likely to be benefited for the excellent soft-magnetic behavior because H_c is expected to be lower than 100 A m^{-1} . Moreover, at low H_c , the M_s ($173.18 \text{ Am}^2 \text{ kg}^{-1}$) and bulk density (97%) are relatively low. Employing three scans using low E ($20\text{--}40 \text{ J mm}^{-3}$) after the first scan using high E ($\geq 60 \text{ J mm}^{-3}$) and low P ($\leq 30 \text{ W}$) could refine the microstructure further (lowering particle size and decreasing the defect concentration), which may achieve the fabrication of high bulk density parts with the superior soft-magnetic properties via the LPBF process. To reduce the particle size, the heat input to the powder layer (energy density) needs to be low, whereas achieving high bulk density and M_s needs a higher energy density. This study indicated that to resolve that conflict, a multiple scanning mechanism is necessary to be applied such as described above.

Acknowledgements

The authors would like to express their very great appreciation to the Republic of Turkey Ministry of National Education for funding this project.

Conflict of Interest

The authors declare no conflict of interest.

Author Contributions

M.G.O.: Conceptualization, methodology, validation, formal analysis, investigation, resources, data curation, writing—original draft, writing—review and editing, visualization, project administration, and funding

acquisition. N.A.M.: Conceptualization, methodology, resources, writing—review and editing, supervision, and project administration.

Data Availability Statement

The data that support the findings of this study are available from the corresponding author upon reasonable request.

Keywords

bulk metallic glasses, Fe-based nanocrystalline alloys, laser additive manufacturing, energy density, laser powder bed fusion, soft-magnetic behavior

Received: May 12, 2023
Revised: September 18, 2023
Published online:

- [1] T. Liu, F. Li, A. Wang, L. Xie, Q. He, J. Luan, A. He, X. Wang, C. Liu, Y. Yang, *J. Alloys Compd.* **2019**, 776, 606.
- [2] O. Gutfleisch, M. Willard, E. Bruck, C. Chen, S. Sankar, J. Liu, *Adv. Mater.* **2011**, 15, 821.
- [3] T. Liu, H. Zhang, F. Kong, A. Wang, Y. Dong, A. He, X. Wang, H. Ni, Y. Yang, *J. Mater. Res. Technol.* **2020**, 9, 3558.
- [4] J. Silveyra, E. Ferrara, D. Huber, T. Monson, *Science* **2018**, 362, aao0195.
- [5] D. Azuma, N. Ito, M. Ohta, *J. Magn. Magn. Mater.* **2020**, 501, 166373.
- [6] H. Li, A. Wang, T. Liu, P. Chen, A. He, Q. Li, J. Luan, C. Liu, *Mater. Today* **2021**, 42, 49.
- [7] M. Cai, J. Wang, Q. Wang, Z. Guo, Q. Luo, J. Zhou, T. Liang, X. Li, Q. Zeng, B. Shen, *Mater. Res. Lett.* **2023**, 11, 595.
- [8] R. Alben, J. Becker, *J. Appl. Phys.* **1978**, 49, 1653.
- [9] G. Herzer, *Acta Mater.* **2013**, 61, 718.
- [10] G. Herzer, *Scr. Metall. Mater.* **1995**, 33, 1741.
- [11] G. Herzer in *Handbook of Magnetic Materials* (Ed: K. H. J. Buschow), Vol. 10, Elsevier, North Holland **1997**, pp. 415–462.
- [12] A. Leary, V. Keylin, A. Devaraj, V. DeGeorge, P. Ohodnicki, M. McHenry, *J. Mater. Res.* **2016**, 31, 3089.
- [13] Y. Ogawa, M. Naoe, Y. Yoshizawa, R. Hasegawa, *J. Magn. Magn. Mater.* **2006**, 304, 675.
- [14] J. Zhang, C. Chang, A. Wang, B. Shen, *J. Non-Cryst. Solids* **2012**, 358, 1443.
- [15] N. Yodoshi, S. Ookawa, R. Yamada, N. Nomura, K. Kikuchi, A. Kawasaki, *Mater. Res. Lett.* **2018**, 6, 100.
- [16] L. Shi, K. Yao, *Mater. Des.* **2020**, 189, 108511.
- [17] A. Setyawan, K. Takenaka, P. Sharma, M. Nishijima, N. Nishiyama, A. Makino, *J. Appl. Phys.* **2015**, 117, 17B715.
- [18] L. Hou, X. Fan, Q. Wang, W. Yang, B. Shen, *J. Mater. Sci. Technol.* **2019**, 35, 1655.
- [19] Q. Luo, D. Li, M. Cai, S. Di, Z. Zhang, Q. Zeng, Q. Wang, B. Shen, *J. Mater. Sci. Eng.* **2022**, 116, 72.
- [20] T. Liu, A. He, F. Kong, A. Wang, Y. Dong, H. Zhang, X. Wang, H. Ni, Y. Yang, *J. Mater. Sci. Technol.* **2021**, 68, 53.
- [21] B. Sharma, X. Zhang, Y. Zhang, A. Makino, *Scr. Mater.* **2015**, 95, 3.
- [22] M. Ohta, Y. Yoshizawa, *Appl. Phys. Express* **2009**, 2, 023005.
- [23] A. Makino, *IEEE Trans. Magn.* **2012**, 48, 1331.
- [24] K. Suzuki, R. Parsons, B. Zhang, K. Onodera, H. Kishimoto, A. Kato, *Appl. Phys. Lett.* **2017**, 110, 012407.
- [25] X. Tong, Y. Zhang, Y. Wang, X. Liang, K. Zhang, F. Zhang, Y. Cai, H. Ke, G. Wang, J. Shen, A. Makino, W. Wang, *J. Mater. Sci. Technol.* **2022**, 96, 233.
- [26] M. McHenry, M. Willard, D. Laughlin, *Prog. Mater. Sci.* **1999**, 44, 291.
- [27] T. Liu, A. He, A. Wang, X. Wang, H. Zhang, H. Ni, *J. Alloys Compd.* **2022**, 896, 163138.
- [28] X. Li, Y. Dong, X. Liu, S. Wu, R. Zhao, H. Wu, W. Gao, A. He, J. Li, X. Wang, *Mater. Sci. Eng. B* **2022**, 285, 115965.
- [29] G. Herzer, *IEEE Trans. Magn.* **1989**, 25, 3327.
- [30] G. Herzer, *IEEE Trans. Magn.* **1990**, 26, 1397.
- [31] K. Suzuki, J. Cadogan, *Phys. Rev. B* **1998**, 58, 2730.
- [32] A. Hernando, P. Marin, M. Lopez, T. Kulik, K. Varga, G. Hadjipanayis, *Phys. Rev. B* **2004**, 69, 052501.
- [33] N. Kone, T. Hua, *J. Energy Power Eng.* **2020**, 14, 100.
- [34] J. Lopez-Sanchez, E. Navarro, A. Serrano, C. Granados-Miralles, A. del Campo, A. Quesada, P. Marin, *ACS Appl. Electron. Mater.* **2020**, 5, 2.
- [35] J. Lopez-Sanchez, E. Navarro, F. Rodriguez-Granado, A. Serrano, P. Marin, *J. Alloys Compd.* **2021**, 864, 158136.
- [36] G. Barrionuevo, J. Ramos-Grez, M. Walczak, X. Sanchez-Sanchez, C. Guerra, A. Debut, E. Haro, *Rapid Prototyping J.* **2022**, 29, 425.
- [37] J. Ravalji, S. Raval, *Rapid Prototyping J.* **2022**, 29, 792.
- [38] M. Khorasani, A. Ghasemi, M. Leary, E. Sharabian, L. Cordova, I. Gibson, D. Downing, S. Bateman, M. Brandt, B. Rolfe, *Opt. Laser Technol.* **2022**, 153, 108263.
- [39] V. Sufiarov, D. Erutin, A. Kanyukov, E. Borisov, A. Popovich, D. Nazarov, *Materials* **2022**, 15, 4121.
- [40] Y. Nam, B. Koo, M. Chang, S. Yang, J. Yu, Y. Park, J. Jeong, *Mater. Lett.* **2020**, 261, 127068.
- [41] L. Zrodowski, B. Wysocki, R. Wroblewski, *J. Alloys Compd.* **2019**, 771, 769.
- [42] M. Ozden, N. Morley, *J. Alloy Compd.* **2023**, 960, 170644.
- [43] M. Ozden, F. Freeman, N. Morley, *Adv. Eng. Mater.* **2023**, 2300597, <https://doi.org/10.1002/adem.202300597>.
- [44] C. Yang, G. Yang, Y. Lu, Y. Chen, Y. Zhou, *Trans. Nonferrous Met. Soc. China* **2006**, 16, 39.
- [45] P. Zhang, J. Tan, Y. Tian, H. Yan, Z. Yu, *Int. J. Adv. Manuf. Technol.* **2022**, 118, 2017.
- [46] J. Lee, Y. Kim, J. Ahn, H. Kim, S. Lee, B. Lee, *Acta Mater.* **2004**, 52, 1525.
- [47] Y. Nam, B. Koo, M. Chang, S. Yang, J. Yu, Y. Park, J. Jeong, *Mater. Lett.* **2020**, 261, 127068.
- [48] S. Alleg, R. Drablia, N. Fenineche, *J. Supercond. Novel Magn.* **2018**, 31, 3565.
- [49] S. Gao, X. Yan, C. Chang, E. Aubry, P. He, M. Liu, H. Liao, N. Fenineche, *Mater. Lett.* **2021**, 290, 129469.
- [50] L. Thorsson, M. Unosson, M. Perez-Prado, X. Jin, P. Tiberto, G. Barrera, B. Adam, N. Neuber, A. Ghavimi, M. Frey, R. Busch, I. Gallino, *Mater. Des.* **2022**, 215, 110483.
- [51] M. Willard, M. Daniil, in *Handbook of Magnetic Materials* (Ed: K. H. J. Buschow), Vol. 21, Elsevier, North Holland **2013**, pp. 173–342.
- [52] S. Sgobba, *CERN* **2010**, 4, 39.
- [53] J. Zhou, J. You, K. Qiu, *J. Appl. Phys.* **2022**, 132, 040702.